

New single-electron pump regime with highly controllable plateaus

Hume Howe (✉ uceehh@ucl.ac.uk)

University College London

Mark Blumenthal

University of Cape Town

Harvey Beere

University of Cambridge

Thomas Mitchell

University of Cambridge

David Ritchie

University of Cambridge <https://orcid.org/0000-0002-9844-8350>

Michael Pepper

University College London

Article

Keywords: quantum based electronic systems, current, single-electron pump mechanism

Posted Date: March 11th, 2021

DOI: <https://doi.org/10.21203/rs.3.rs-294506/v1>

License:  This work is licensed under a Creative Commons Attribution 4.0 International License.

[Read Full License](#)

New single-electron pump regime with highly controllable plateaus

H. Howe*¹, M. Blumenthal*², H. E. Beere³, T. Mitchell³, D. A. Ritchie³, and M. Pepper¹

¹University College London, London Centre for Nanotechnology and Dept. of EE, London, WC1A 0AH, U.K.

²University of Cape Town, Physics Dept., Rondebosch, 7700, South Africa

³University of Cambridge, Physics Dept., Cavendish Laboratory, Cambridge, CB3 0HE, U.K.

*These authors contributed equally to this work.

ABSTRACT

Future quantum based electronic systems will demand robust and highly accurate on-demand sources of current. Generating quantised current has immediate implications for quantum computing, quantum metrology, and electron interferometry. The ultimate limit of quantised current sources is a highly controllable device that manipulates individual electrons. We present a new single-electron pump mechanism, realised in a GaAs two-dimensional electron gas, where electrons are pumped through a one-dimensional split-gate confinement potential rather than more conventionally over a finger-gate potential. This new mechanism yields a new long pumping regime with quantised plateaus that are over two orders of magnitude longer than conventional pumps, and are extremely stable with respect to the applied voltages on the gates. The long plateaus are achieved via the combination of a saddle-point potential profile and enhanced quantum tunnelling, wherein the potential barrier height and shape are modified by the application of a source-drain bias. This new pumping regime cannot be explained by the simple geometrical electrostatic models or back-tunnelling theory that are used to describe conventional single-electron pumps, and we use a simple electrostatic model applied to split-gate confined pumps to explain some of the source-drain bias dependence.

Main

The field of quantum technology that is dependent on quantised current sources has grown considerably in the past two decades. Single-electron pumps allow for the on-demand supply of electrons with a high degree of precision. These pumps are promising building-blocks for solid-state quantum computation based on electron-quantum-optic devices¹⁻³, where the pump is used as a controllable electron source incident on electrostatic barriers, analogous to passing photons through beam splitters. In the metrology community, single-electron pumps are the leading contender for the redefinition of the SI unit, Ampere, where the produced current is defined in terms of the fundamental charge of the electron e ⁴. In both applications, robust and tunable on-demand pumping is essential.

Initially, electron-counting devices, based on resonant tunnelling through a quantum dot (QD)⁵, were frequency limited by the need for the system to be adiabatic⁶. This was overcome with the demonstration of dynamic QD pumps, where a three-gated electrostatically defined QD is created and destroyed each cycle⁷. This was later revised to a simpler two-gated ratchet style pump, which has widely been adopted as the mechanism for producing high accuracy on-demand single-electron current^{8,9}. Comprehensive reviews are given by Giblin *et al.* and Baurle *et al.*^{10,11}. In the ratchet style pump, two electrostatic gates, labelled Entrance gate and Exit gate, are patterned on a two-dimensional electron gas (2DEG) substrate and define a QD. A negative voltage is applied to the Exit gate to separate the 2DEG channel into a source and drain. An oscillating voltage is coupled to the Entrance gate such that a QD forms on the source side, trapping electrons from the Fermi level, and raising the trapped electrons high enough to eject over the Exit gate.

Current is quantised at $I = nef$, where n is the number of electrons pumped per cycle, e is the electron charge, and f is the driving frequency. In practice, the measured current deviates from the ideal $I = nef$ due to errors associated with back-tunnelling^{12,13}.

Our pump is a ratchet-style pump, but utilises a split-gate as the exit gate. This introduces a saddle point potential that strongly effects the measured current. When large enough DC voltage, RF amplitude, or source-drain bias is applied, the measured current becomes extremely stable with respect to the Exit gate voltage. With the plateau length defined in terms of fitting parameters to the universal decay cascade model^{12,13} (UDC), the plateaus can be over two orders of magnitude longer than those of conventional pumps and turnstiles. This new pumping regime we call the long pumping regime (LPR), to distinguish it from the pumping regime of conventional pumps and turnstiles that operate in what we call the conventional pumping regime (CPR). We discuss the different regimes by the change in interdependencies of the applied gate voltages (V_{Ent}

and V_{Exit}), source-drain bias voltage (V_{bias}), and RF amplitude (RF_{Amp}) on the measured pumped current (I).

The CPR interdependencies are that the plateau length is independent on V_{bias} , changes linearly with RF_{Amp} , and where the parameter in a UDC fit that gives the curvature of the transition (α) between the plateaus, remains constant. This resembles pumps in previous literature. In the LPR, the plateau length changes exponentially with V_{bias} , exponentially with RF_{Amp} , and α decreases for higher plateaus. When operating in the LPR, both the control of the source-drain bias and RF amplitude allows for an increase in the plateaus length, width, and flatness.

Results

Measurement circuit

Figure 1(a) shows a false-colour scanning electron microscope (SEM) image of one of the pump devices and a schematic of the measurement setup. The device is made up of an etched 2DEG channel with a surface finger-gate (entrance gate) and split-gate (exit gate) defining the QD pump geometry. Voltages were applied to the gates using an external digital to analogue converters (DACs) with an RF voltage component added to the entrance gate with an external bias-tee. The device was encased in a sample holder with electromagnetic interference (EMI) protection and placed in a dilution refrigerator. Details of the 2DEG wafer and measurement circuit with EMI protection are given in the [Methods](#). Figure 1(b) shows an artists depiction of the saddle point potential (green) at the 2DEG formed by the split-gate pump. The form of this potential is modelled in section [Gate modelling](#), where it is compared to standard finger-finger gate potential profiles.

Source-drain bias dependence of LPR

The source-drain dependence of the pumped current shows the differences between the CPR and LPR. Measuring current vs V_{Exit} and V_{Ent} , we create a 2D colour-map 'pumpmap' from which we investigate the different pumping regimes. All data is taken at $T = 45$ mK, with no magnetic field ($B = 0$ T), $\text{RF}_{\text{Amp}} = 220$ mV, and $f = 180$ MHz. Pumping was also seen at a range of other frequencies (including higher frequencies) as is the case when operating in the CPR.

Figure 2(a) shows derivative pumpmaps at different V_{bias} . The white numbers in the dark blue plateau regions show the number of electrons pumped. The light blue lines show the transition between plateaus. The plateaus are enclosed by onset (solid grey), ejection (dashed green), and capture (dashed yellow) lines, all of which mark the transition from no pumped current to quantised pumping. The first onset line on the left of each pumpmap indicates the onset of pumping of a single electron and each subsequent onset line indicates the pumping of an additional electron. In the thermal regime, the first onset line marks the transition where a dot, of size determined by the gate voltages intersecting the onset line, forms at the Fermi level. The ejection lines mark where V_{Ent} is negative enough to push the electron over the split-gate potential. Only the ejection line that corresponds to the first plateau in each pumpmap is shown. The ejection lines are extended across each pumpmap as a point of reference for comparing the pumpmaps. Apart from a small slope, likely due to cross-talk between the gates, the ejection lines are independent of V_{Exit} . The capture line marks where V_{Ent} is negative enough such that the dot forms below the Fermi level. The first plateau has a plateau width (purple arrow) between the capture and ejection lines, and a plateau length (red arrow) between the onset lines of the first and second plateau. The purple 'X' in figure 2(a) and (b) are regions where Ohmic current dominates the pumped current. This region is shown as flat (derivative is approximately zero) as the high Ohmic current saturates the electrometer on the measurement range used.

The pumpmap at $V_{\text{bias}} = -60$ mV is in the CPR. The onset lines are straight and the plateau is ≈ 30 mV long. As the pump is forward biased (V_{bias} is made more positive) the onset lines becomes curved and the the plateaus lengthen, while the plateau widths remain fixed, independent of V_{bias} . The pumpmap at $V_{\text{bias}} = 60$ mV shows the pump already operating in the LPR with the pumpmap at $V_{\text{bias}} = 120$ mV showing a markedly increased plateau length of ≈ 600 mV long. Previously, the the only in-situ controllable parameter for increasing the length of a plateau was to operate the pump in a high magnetic field, as is the standard operating regime when for metrological studies of quantum pumping. However, the physical mechanism that governs this magnetic field interaction is not well understood. Figure 2(b) shows a derivative pumpmap of current vs V_{Exit} and V_{bias} . The schematics shown on each corner are cartoon depictions of the relative potentials of the source, entrance gate, exit gate, and drain, corresponding to the four quadrants of the pumpmap. The entrance gate potential is shown in red with the exit gate potential shown in green. In figure 2(b), the LPR-CPR transition region is given by the two red dashed lines. To the right of this region, at $V_{\text{Exit}} > -910$ mV, the plateau length is only weakly dependent of V_{bias} . As V_{bias} is increased, the plateaus shift approximately linearly to more negative V_{Exit} values. In contrast, to the left of the LPR-CPR transition region, at $V_{\text{Exit}} < -930$ mV, the plateau length increases exponentially with increased V_{bias} and the plateaus shift to exponentially more negative V_{Exit} . At a given V_{Exit} , the quantised pumping can be observed in the LPR by increasing V_{bias} until the long first plateau is revealed along the $n = 0$ to $n = 1$ plateau transition in figure 2(b). As the transition flattens off in V_{Exit} exponentially, very long quantised plateaus can be generated. Line scans with $\text{RF}_{\text{Amp}} = 400$ mV and $V_{\text{Ent}} = -300$ mV, are shown in figure 2(c). Our investigation was restricted to a maximum voltage applied to the split gate of -18 V (-9.5 V shown here), but currently no upper limited has been determined for the length of plateau as a function of split-gate voltage in the LPR.

RF amplitude dependence of LPR

The RF amplitude of the driven finger-gate is another parameter that changes whether the pump is operating in the CPR or LPR. Figure 3(a) shows pumpmaps at different RF amplitudes, with fixed $V_{\text{bias}} = 60$ mV. At $\text{RF}_{\text{Amp}} = 100$ mV, the pump is in the CPR. The pumpmap resembles that of conventional pumps comprising of two finger gates, with straight onset lines and a plateau length ≈ 30 mV. As the RF_{Amp} increases, the onset lines become curved with the first onset line becoming more curved than the second onset line. At $\text{RF}_{\text{Amp}} = 200$ mV the pump is in the LPR, with plateau length ≈ 420 mV. As RF_{Amp} is further increased the onset lines don't move, and the plateau length at a given V_{Ent} remains constant. As RF_{Amp} increases the plateau width increases linearly, pushing out the capture and ejection lines equally. Figure 3(b) is a derivative plot showing how the plateau width increases linearly with increasing RF_{Amp} . Equation 1 relates the plateau width to the applied RF amplitude.

$$\text{Plateau width} = 3.5 \times (\text{RF}_{\text{Amp}} - 125 \text{ mV}) \quad (1)$$

The plateau width is larger than the applied RF amplitude, which is attributed to the cross coupling of the gates. This linear dependence agrees with previous literature on pumps in the CPR¹⁴.

The plateau length change is a defining characteristic of the LPR. Figure 3(c) is a derivative plot of current vs V_{Exit} and RF_{Amp} . As RF_{Amp} increases, the plateau length at fixed V_{Exit} initially increases linearly until $\text{RF}_{\text{Amp}} \approx 160$ mV, at which point it increases exponentially and saturates when $\text{RF}_{\text{Amp}} \approx 200$ mV. The horizontal dashed red line separates the CPR from the LPR. Because the onset line is curved and remains fixed we can measure longer plateau lengths at less negative V_{Ent} .

In our split-gate pumps, changing RF_{Amp} at a fixed V_{Ent} only changes the plateau width without a change in the plateau length. Also, changing V_{bias} changes the plateau length without changing the plateau width. Combining these allows for a new level of control not seen before in conventional pumps. Figure 4 is a derivative pumpmap of current vs V_{bias} and RF_{Amp} at fixed $V_{\text{Ent}} = -300$ mV and $V_{\text{Exit}} = -1200$ mV. The number of pumped electrons are shown in white. The pumpmap shows an unexpected structure at the boundary of not-pumping to pumping (red dashed line). This structure is similar in shape to the boundary of not-pumping to pumping in the ejection lines of a V_{Exit} and V_{Ent} pumpmap, suggesting that the V_{bias} and RF_{Amp} have a similar effect on the ejection process or the dot size at some key points in the pumping cycle. The changing effect that V_{bias} and RF_{Amp} have on the potentials at the exit and entrance gates may be equivalent to changing V_{Exit} and V_{Ent} directly. The lighter blue vertical line near $V_{\text{bias}} = 0$ mV appears to be a measurement artefact.

Discussion

Plateau fitting

There are a few theoretical models that describe a possible mechanism for conventional quantised pumping^{2,12,15}, with a good summary and the relative merits and limitations discussed by Giblin *et al.*¹⁶. Flatness for metrology needs to be done empirically, as fits do not necessarily capture all the error mechanisms in the pumping process, and currently there is no theoretical framework that describes all the error mechanisms and provides a good fit to the data. The most commonly used model has been the universal decay cascade (UDC) back-tunnelling model¹². It has been used to parameterise quantised pump data and extract a 'fingerprint of flatness', that gives an indication of how flat a pump plateau is, and thus its potential usefulness for more in-depth empirical metrological study. The UDC model takes the form of a double exponential fitting equation

$$I = (ef) \sum_n \exp[-\exp(-\alpha_n(V_{\text{Exit}} + \delta_n))] \quad (2)$$

where α_n and δ_n are fitting parameters over n plateaus. In equation 2, α_n gives the curvature of the rise from the $n - 1$ th to the n th plateau, with a large α_n being more step-function-like. δ_n are locations in V_{Exit} of the transition between plateaus $n - 1$ and n . Note that our use of α_n and δ_n differ slightly from that quoted in past UDC literature, which use $I = (ef) \sum_n \exp[-\exp(-\alpha V_{\text{Exit}} + \Delta_n)]$, with $\Delta_n = \alpha \times \delta_n$. Here α is written as factored out of the exponent, so the plateau length can be defined as $PL_n = \delta_n - \delta_{n-1}$, which is independent of α . According to Giblin *et al.*, the difference $\Delta_2 - \Delta_1$ is commonly used as a figure of merit for flatness of the first plateau, with larger $\Delta_2 - \Delta_1$ corresponding to a flatter plateau¹⁰. While this can be used to compare plateaus with either constant curvature or constant plateau length, it cannot be used to compare devices where both curvature and plateau length change, as is the case in the LPR. Figure 5(a) shows UDC fits of equation 2 (red lines) to linescans of pumped current in the LPR for $V_{\text{bias}} = 60$ mV (green) and $V_{\text{bias}} = 0$ mV (blue). α_n and δ_n remain as fitting parameters only, without a physical counterpart except as a representation for an ensemble of measurement errors. If an equation can be found that accurately fits the data, and fits when parameters are changed, we can infer that it accounts for the error mechanisms associated with those parameters. Unfortunately, the UDC model does not accurately fit the data: it under-counts electrons at the start (1) and end (3) of the rise from $n = 0$ to $n = 1$, while over-counting electrons in the

middle of the rise (2). This is the case for all fits, including in the CPR, and is a consequence of defining the curvature to the left and right of δ_1 with one parameter, α . Figure 5(b) shows how α and the plateau length change with V_{bias} . The plateau length appears to increase exponentially and when fitting to the long plateau data in figure 2(c), the plateau length as defined by the UDC fit is 10.26 V. This is over two orders of magnitude longer than conventional pumps, which have lengths in the tens to hundreds of mV range. However, because the plateaus at increased V_{bias} are both longer and shallower, a 'fingerprint' of flatness cannot be determined by multiplying the curvature and plateau length parameters. Instead, we measure the slope directly by taking numerical derivative from the data. Figure 5(c) shows the minimum slope from linescans at different V_{bias} , with data taken in the region of the pump near the corner of the ejection and 2nd onset line, shown by the red circle in figure 2(a). Note that this data has a V_{Exit} step size of 5 mV measured on a 1 nA range, which results in a larger change in current than the noise level of the electrometer. When measuring with a small step size the current noise can be greater than the change in current per step in V_{Exit} , so a direct measurement in the change of slope cannot be used without modification. However, as V_{bias} increases and the pumping regime migrates from the CPR to LPR the slope clearly decreases: from $6.1\text{E-}4$ ef/mV at $V_{\text{bias}} = -65$ mV to $3.3\text{E-}5$ ef/mV at $V_{\text{bias}} = 95$ mV. Beyond this the slope becomes comparable to the noise at this level and we cannot easily resolve a slope without first smoothing the data. While precise measurements of flatness require a dedicated metrological measurement setup, these measurements show that split-gate pumps and control of V_{bias} appear promising for future metrological based experiments.

Voltage to energy relationship

The extremely long plateaus observed in the LPR offers the experimentalist a range of ejection energies proportional to the voltage applied to the exit split-gate. The lever arm term, usually denoted α (different to the UDC α discussed earlier), maps the applied gate voltage on the split gate, to a potential energy by $E = \alpha \times V + \text{offset}$. In a pumping process it allows for the energy of electrons ejected from the pump to be determined. The lever arm term is detailed in ref.¹ and explained briefly here. When a large enough negative voltage is applied to a gate across a biased etched channel such that the 2DEG is completely pinched off, it is assumed that the entire source-drain voltage (V_{bias}) is dropped across the pinched-off gate, such that the potential energy at the 2DEG is given by $e \times V_{\text{bias}}$. By increasing the gate potential to more positive values until current is allowed to flow, we get a mapping of the applied gate voltage to the energy at the 2DEG. Applying this technique to a pump device, which has two gates, is problematic due to cross-talk that exists from the pickup of background RF and transient voltage spikes on the unfiltered gate even when one of the gates is grounded. One way of addressing this is to create a second device with only the split gate. This does not give a realistic picture of how the lever arm term may change when an RF signal is applied to an adjacent finger gate. Figure 6 shows the mapping of V_{Exit} to V_{bias} taken on a split-gate finger-gate pump device with the $\text{RF}_{\text{Amp}} = 220$ mV to ensure that we account for the cross-talk that occurs between the gates. We can separate out a DC lever arm term from the change in offsets for the split-gate pinch-off profiles. This is shown by the dashed white lines in the CPR, where gate pinch-off is symmetrical about $V_{\text{bias}} = 0$. The energy voltage relationship can be approximated by

$$E_{\text{CPR}} = e \times [-0.4 \times V_{\text{Exit}} - 280 \text{ mV}] \quad (3)$$

for $-700 \text{ mV} > V_{\text{Exit}} > -1000 \text{ mV}$.

As V_{Exit} is made more negative, the increase in energy is no longer linear and pinch-off lines become asymmetric in V_{bias} . While it continues to be linear for $V_{\text{bias}} > 0$, it curves for $V_{\text{bias}} < 0$. In the far LPR ($-4000 \text{ mV} > V_{\text{Exit}}$), this can be approximated linearly again (dashed green line) by

$$E_{\text{LPR}} = e \times [-0.002 \times V_{\text{Exit}} + 152 \text{ mV}]. \quad (4)$$

Pumping with $V_{\text{Exit}} = -4000$ mV would have a corresponding peak barrier energy of 160 meV. This energy is the average height, of the exit barrier together with any cross talk from the oscillating entrance barrier, above the Fermi-level in the source, and is comparable to measured ejection energy in the literature of $> 150 \text{ meV}$ ¹ for a finger gate pump at $V_{\text{Exit}} \approx -500$ V with $V_{\text{bias}} < 10$ mV. However in our device, to pump electrons at $V_{\text{Exit}} = -4000$ mV, V_{bias} needs to be greater than ≈ 110 mV. A difficulty in using V_{bias} to calibrate the energy of gate-defined potential barriers is that the potential at the gate is not independent of V_{bias} . Figure 6(b) shows the variation of the potential energy of the QPC for different bias voltages. As the Fermi level at the drain is lowered, the peak energy is pulled down and forward tunnelling is enhanced¹⁷. The energy of the pumped electrons are assumed to be near the peak energy of the barrier, which can be calculated with a simple electrostatic model, or measured directly in a device that incorporates a second barrier that can be calibrated to its own V_{bias} , as done by Fletcher et. al.¹.

Due to the very small slope of the LPR lever arm term in equation 4 and the relatively large slope of the CPR lever arm term in equation 3, the ejected energies can be finely chosen within a small energy range (≈ 10 meV) over a large gate voltage range

(≈ 4000 mV) or more coarsely chosen withing a larger energy range (≈ 120 meV) over a large gate voltage range (≈ 300 mV). This allows for a level of control that covers a large range of energies with varying levels of precision, and highlights the importance of V_{bias} in the selection of ejected electron energies, making these pumps promising single electron sources for quantum-optics experiments¹⁸.

Gate modelling

Source-Drain Bias Effects

In finding a physical mechanism for the source-drain dependence observed in the LPR, we examine previous literature on QPC gate potentials under source-drain bias, which shows that the bias has a direct influence on the effective gate potentials and tunnel current^{19,20}. We invoke a model detailed by Gloos *et al.*²¹, where a hard-wall potential with eigen energies given by

$$E_n[w(x)] = \frac{n^2 h^2}{8m^* w^2(x)} \quad (5)$$

is utilised instead of a more conventional saddle-point approximation. Here h is Planck's constant, $m^* = 0.067m_e$ is the effective electron mass in GaAs, the index n denotes the different 1D subbands, and $w(x)$ is the width of the constriction approximated by an inverted Gaussian given by

$$w(x) = w_0 \exp\left(-\frac{x^2}{L^2}\right). \quad (6)$$

Here, w_0 is the minimum width of the unbiased constriction at a fixed gate voltage, and L defines its length.

In the far pinched-off regime, the applied source-drain bias changes the barrier energy as seen by the electrons in the 2DEG. This change in electrostatic energy is approximated by

$$E_{\text{bias}}(x) \approx -\frac{eV_{\text{bias}}}{2} \left[1 + \tanh\left(\frac{5x}{2L}\right) \right], \quad (7)$$

which is added to the eigen energies given by equation 5.

Figure 6(b) shows the variation of the potential energy of the QPC using the sum of equations 5 and 7, with the $V_{\text{bias}} = -100$ mV (green), 0 mV (yellow) and 100 mV (blue). The bias voltage changes the maximum height of the QPC potential as well as shifts the position of this maximum along the channel, changing the effective size of the quantum dot. As the potential of the drain with respect to the pumped electrons is lowered, the size of the dot formed during each pump cycle is increased and the height of the exit barrier is lowered. This results in longer plateaus and the formation of the LPR, empirically observed in figure 2(a). If the applied source-drain bias is of the order of several mV, the energy dependence of the density of states of the 1D channel formed by the split-gate can not be neglected. This is especially true when the source-drain bias is greater than the spacing of the quasi-1D subbands produced by the split gate. In this regime, the conductance is non-linear due to the asymmetry in the number of subbands available for transport in the forward and reverse direction. Gloos *et al.*²¹ indicate that this regime of transport is due to quantum tunnelling through the saddle-point potential and not thermal effects due to local heating from the applied source-drain.

Gate Geometry Effects

We present a simple model to detail the difference between the electrostatic potential established due to the new gate geometry of a split-gate, finger gate pump that operates in this new LPR to that obtained in the CPR with a standard finger-finger gate designed pump. It is normally useful to start from a discussion of the form of the self-consistent potential that arises for electrons when a gate bias is applied. However, we present an analytical calculation where the effects due to space charge layer formation is neglected and the GaAs/AlGaAs heterostructure is treated as a dielectric²². For two metallic electrodes held at a constant gate voltage V_g , forming a narrow constriction, the confining potential is expressed as:

$$V(x, y) = f\left[\frac{2x-l}{2z_0}, \frac{2y+w}{2z_0}\right] - f\left[\frac{2x+l}{2z_0}, \frac{2y+w}{2z_0}\right] + f\left[\frac{2x-l}{2z_0}, \frac{-2y+w}{2z_0}\right] - f\left[\frac{2x+l}{2z_0}, \frac{-2y+w}{2z_0}\right] \quad (8)$$

where

$$f(u, v) = \frac{eV_{\text{gc}}}{2\pi} \left[\frac{\pi}{2} - \tan^{-1} u - \tan^{-1} v + \tan^{-1} \frac{uv}{\sqrt{1+u^2+v^2}} \right] \quad (9)$$

Here, l and w are the lithographic width and gap between the electrodes respectively, V_{gc} is the calibrated (see below) applied gate voltage and z is the vertical distance between the 2DEG and the gate. In this case the split gate $l = 400$ nm and $w = 400$ nm, whilst for all finger gates modelled, $l = 230$ nm.

As discussed in Davies *et al.*²² we ignore electron screening in the vicinity of the quantum dot as the device is operated in the far pinch-off regime where the local 2DEG is depleted. There has been much discussion on the behaviour of the exposed surfaces (boundary conditions) around the gates when utilising such analytical techniques for modelling²³. It can be assumed that the Fermi energy E_F is pinned at a fixed energy below the conduction band on the free surface of the top GaAs layer²⁴. This fixed energy is normally taken as the zero of energy and potential. In this "pinned" surface boundary condition, the exposed surface acts as an equipotential at zero. However, in-order to keep the potential constant in response to a change in V_g , charge must move from the 2DEG to the surface. At low temperatures this required charge flow may not be possible. Alternatively, the surface could be treated as a simple dielectric boundary, where the charge density is fixed to the charge density in the donor layer in response to a change in V_g on the gates²⁵. This is known as the "frozen" surface boundary condition. This too may be problematic as the patterned gates may produce strong horizontal electric field components which could change the occupation of donors.

Here, as detailed in Davies *et al.*²², we circumvent the issues with both the "pinned" and "frozen" boundary conditions by not invoking any of the gate voltage correction terms, but calibrate the gate voltages to the experimental threshold voltages (pinch-off voltages) for both the finger and split gates. Making use of the electron density of the heterostructure $n_{2D} = 1.5 \times 10^{15} \text{ m}^{-2}$, the threshold voltage can be obtained from the following expression:

$$V_t = \frac{-en_{2D}z}{\epsilon_r \epsilon_0} \approx -466 \text{ mV}. \quad (10)$$

Here, e is the charge of the electron, $\epsilon_r = 11.963$ the dielectric constant of AlGaAs and z the vertical distance between the 2DEG and the gate. When determining z , the distance from the surface to the peak density of trapped electrons should be taken which is approximately 10 nm deeper than the start of the well itself. Here $z = 100$ nm.

Experimentally, the threshold voltages for the finger gate and split gate are found to be -350 mV and -748 mV respectively, resulting in a proportional calibration factor for the split gate $k_{\text{sg}} = 1.604$ and finger gate $k_{\text{fg}} = 0.750$. We therefore have the following expression for the calibrated applied gate voltage:

$$V_{\text{gc}} = \begin{cases} k_{\text{sg}} V_g & \text{for split gate,} \\ k_{\text{fg}} V_g & \text{for finger gate.} \end{cases} \quad (11)$$

where V_g is the voltage set by the data acquisition system for either a Exit finger gate or Exit split gate.

The potential energy profiles for the finger-finger gate pump geometry (CPR) and finger-split gate pump geometry (LPR) calculated from (8) are given in figure 7(a) and (c) respectively. We choose voltages that correspond to the voltages used in our device in the LPR, $V_{\text{Exit}} = -4000$ mV and $V_{\text{Ent}} = -1500$ mV, where V_{Ent} corresponds to the combined DC voltage and RF amplitude where the entrance gate reaches a maximum. The final voltage values inserted into (8) are first corrected for, by making use of (11). At these unusually large voltages for finger-finger gate pumps, there is no sign of a quantum dot and no obvious exit path to the drain. It can be seen that with a split-gate, a saddle point is formed with a pronounced quantum dot, and there is an exit path to the drain. Cross section plots of both gate geometry potential energies along the $y = 0$ line are shown in figure 7(a) and 7(d). For the finger-split gate geometry, the position of the maximum potential energy along the $y = 0$ line is found at $x = 5.076 \times 10^{-7}$ m, within the region of the entrance plunger gate. It is thus favourable for the electron to leave through the exit split gate centred at $x = 0$ m. For the finger-finger gate geometry, the position of the maximum potential energy along the $y = 0$ line is found at $x = 2.820 \times 10^{-9}$ m, within the physical boundary of the exit gate and therefore blocking any exit path for the electron. The clear differences in the potential energy profiles between the two gate geometries informs on why the LPR has not been observed previously in conventional finger-finger gate pumps (CPR) and demonstrates the novelty of implementing these non-adiabatic pumps with a large exit split gate.

Conclusion

This new long and robust plateau regime, the result of a simple design change to the gates defining the dynamic QD, allows single electron pumps to be tuned by a source-drain bias, which adds a new experimental parameter leading to the emergence of the LPR. This source-drain bias dependence, together with the RF amplitude dependence, gives researchers in the fields of quantum information and metrology two experimental parameters for maximising the robustness of single electron pumping in both gate voltages defining the QD. The design changes are unobtrusive and still allow for the ability to integrate our LPR device into more complicated quantum based electronic systems and more sophisticated high-accuracy measurement setups. Initial results indicate a substantial improvement in the minimum slope when increasing V_{bias} , measured on a standard non-metrological grade measuring system. To improve on accuracy, these pumps could be measured by metrological institutes incorporating years of new advancement in measuring techniques, coupled with highly calibrated traceable instruments, which are only readily available to a select few laboratories²⁶. There, these pumps have the potential to be tuned into regions of highly accurate current that previously have been inaccessible. This new design of pump when utilised in a range of studies such as Fermion quantum-optic and quantum computing effects, where the experiment may limit the allowed range of control parameters, may compensate by offering additional robust parameters that place the pump in the desired quantised pumping regime. This new design of pump and operational regime could be extended to other materials such as silicon and graphene.

Methods

The devices were fabricated on MBE grown high mobility GaAs/Al_xGa_{1-x}As Si-doped 2DEG wafers with the 2DEG 90 nm below the surface (10 nm GaAs cap, 40 nm Si-doped GaAs/Al_xGa_{1-x}As, 40 nm GaAs/Al_xGa_{1-x}As spacer, and GaAs substrate) carrier density $n = 1.9\text{E}11 \text{ cm}^{-2}$, mobility $\mu = 1.014\text{E}6 \text{ cm}^2/\text{Vs}$. The 2DEG channel pattern was defined using electron-beam lithography (EBL) and etched to a depth of 40 nm using wet chemistry. The gates were defined using EBL and deposited with 120 nm of Ti/Au in a thermal evaporator. The devices were made more resistant to electromagnetic interference (EMI) by eliminating any areas where there could have been large resistance changes along the gates: this was done by making the gates smooth curves and putting down a thicker Ti/Au layer to easily climb the etched channels.

The devices were loaded into a Leiden Cryogenics dilution fridge with a base temperature of 7 mK and containing a 10 T superconducting magnet. Outside the fridge, current was measured using a Keithley 6430 source measure unit (SMU), which was connected to the drain side of the pump. A NI2969 cDAQ provided the voltages that were applied to the gates. The RF source was a HP E4400B.

To protect the device from EMI, 2 gate filters are used. One is a room-temperature T-filter with 200 k Ω resistors and a 100 pF capacitor. The second a Semtech ECLAMP2458P, which is located right next to the sample on the sample holder PCB; protects the sample when handling it at room-temperature but freezes out at low temperatures providing a normal through contact. No filters were used on the Ohmics and the RF-lines to keep the circuit simple.

Measurement accuracy was improved by using an internally shielded cable from the fridge to the break-out box and by averaging repeat measurements on the Keithley 6430. Averaging over 500 points, the noise was reduced to $< 3 \text{ fA}$ on a 100 pA range. At this range we did not see any drift in the zero current over weeks of measuring. While this is not as accurate a measurement setup as used by dedicated metrology centres, it is sufficient to show the relative benefits of the new pumping regime.

Acknowledgements

This work was supported by the UK Engineering Physical Sciences Research Council, grants EP/K004077/1, EP/R029075/1, EP/P021859/1, the National Research Foundation of South Africa and Sasol. WE would also like to acknowledge a fruit-full discussion with M. Kataoka, S. Giblin, and J. Fletcher at the National Physical Laboratory.

Author contributions statement

H.H. and M.B. conceived the experiment, setup and ran the measurements, analysed and interpreted the data, and wrote the article. H.H. designed and processed the devices and produced the plots and figures. T.M carried out the ebeam lithography. H.E.B and D.A.R developed and grew the GaAs/AlGaAs heterostructures used. M.P. provided support, references, and useful discussions. All authors reviewed the manuscript.

Additional information

The authors declare no competing interests.

References

1. Fletcher, J. D. *et al.* Clock-controlled emission of single-electron wave packets in a solid-state circuit. *Phys. Rev. Lett.* **111**, 216807, DOI: [10.1103/PhysRevLett.111.216807](https://doi.org/10.1103/PhysRevLett.111.216807) (2013).
2. Johnson, N. *et al.* Ultrafast voltage sampling using single-electron wavepackets. *Appl. Phys. Lett.* **110**, 102105, DOI: [10.1063/1.4978388](https://doi.org/10.1063/1.4978388) (2017). <https://doi.org/10.1063/1.4978388>.
3. Ubbelohde, N. *et al.* Partitioning of on-demand electron pairs. *Nat. Nanotechnol.* **10**, 46–49, DOI: [10.1038/nnano.2014.275](https://doi.org/10.1038/nnano.2014.275) (2015).
4. Giblin, S. P. *et al.* Towards a quantum representation of the ampere using single electron pumps. *Nat Commun* **3**, 930, DOI: [10.1038/ncomms1935](https://doi.org/10.1038/ncomms1935) (2012).
5. Kouwenhoven, L. P., Johnson, A. T., van der Vaart, N. C., Harmans, C. J. P. M. & Foxon, C. T. Quantized current in a quantum-dot turnstile using oscillating tunnel barriers. *Phys. Rev. Lett.* **67**, 1626–1629, DOI: [10.1103/PhysRevLett.67.1626](https://doi.org/10.1103/PhysRevLett.67.1626) (1991).
6. Keller, M. W., Martinis, J. M., Zimmerman, N. M. & Steinbach, A. H. Accuracy of electron counting using a 7-junction electron pump. *Appl. Phys. Lett.* **69**, 1804–1806, DOI: [10.1063/1.117492](https://doi.org/10.1063/1.117492) (1996).
7. Blumenthal, M. D. *et al.* Gigahertz quantized charge pumping. *Nat. Phys.* **3**, 343–347 (2007).
8. Kaestner, B. *et al.* Single-parameter nonadiabatic quantized charge pumping. *Phys. Rev. B* **77**, 153301 (2008).
9. Fujiwara, A., Nishiguchi, K. & Ono, Y. Nanoampere charge pump by single-electron ratchet using silicon nanowire metal-oxide-semiconductor field-effect transistor. *Appl. Phys. Lett.* **92**, 042102, DOI: [10.1063/1.2837544](https://doi.org/10.1063/1.2837544) (2008).
10. Giblin, S. P. *et al.* Evidence for universality of tunable-barrier electron pumps. *Metrologia* **56**, 044004, DOI: [10.1088/1681-7575/ab29a5](https://doi.org/10.1088/1681-7575/ab29a5) (2019).
11. Bäuerle, C. *et al.* Coherent control of single electrons: a review of current progress. *Reports on Prog. Phys.* **81**, 056503, DOI: [10.1088/1361-6633/aaa98a](https://doi.org/10.1088/1361-6633/aaa98a) (2018).
12. Kashcheyevs, V. & Kaestner, B. Universal decay cascade model for dynamic quantum dot initialization. *Phys. review letters* **104**, 186805 (2010).
13. Kashcheyevs, V. & Timoshenko, J. Quantum fluctuations and coherence in high-precision single-electron capture. *Phys. review letters* **109**, 216801 (2012).
14. Kaestner, B. *et al.* Robust single-parameter quantized charge pumping. *Appl. Phys. Lett.* **92**, 192106, DOI: [10.1063/1.2928231](https://doi.org/10.1063/1.2928231) (2008).
15. van der Heijden, J., Tettamanzi, G. C. & Rogge, S. Dynamics of a single-atom electron pump. *Sci. Reports* **7**, 44371, DOI: [10.1038/srep44371](https://doi.org/10.1038/srep44371) (2017).
16. Giblin, S. *et al.* Realisation of a quantum current standard at liquid helium temperature with sub-ppm reproducibility. *arxiv* (2019). [1912.02042](https://arxiv.org/abs/1912.02042).
17. Ferry, D. K., Goodnick, S. M. & Bird, J. *Transport in Nanostructures* (Cambridge University Press, 2009), 2 edn.
18. Hong, C. K., Ou, Z. Y. & Mandel, L. Measurement of subpicosecond time intervals between two photons by interference. *Phys. Rev. Lett.* **59**, 2044–2046, DOI: [10.1103/PhysRevLett.59.2044](https://doi.org/10.1103/PhysRevLett.59.2044) (1987).
19. Kouwenhoven, L. P. *et al.* Nonlinear conductance of quantum point contacts. *Phys. Rev. B* **39**, 8040–8043, DOI: [10.1103/PhysRevB.39.8040](https://doi.org/10.1103/PhysRevB.39.8040) (1989).
20. Patel, N. K. *et al.* Ballistic transport in one dimension: additional quantisation produced by an electric field. *J. Physics: Condens. Matter* **2**, 7247–7254, DOI: [10.1088/0953-8984/2/34/018](https://doi.org/10.1088/0953-8984/2/34/018) (1990).
21. Gloos, K. *et al.* Current-voltage characteristics of quantum-point contacts in the closed-channel regime: Transforming the bias voltage into an energy scale. *Phys. Rev. B* **73**, 125326, DOI: [10.1103/PhysRevB.73.125326](https://doi.org/10.1103/PhysRevB.73.125326) (2006).
22. Davies, J. H., Larkin, I. A. & Sukhorukov, E. V. Modeling the patterned two-dimensional electron gas: Electrostatics. *J. Appl. Phys.* **77**, 4504–4512, DOI: [10.1063/1.359446](https://doi.org/10.1063/1.359446) (1995). <https://doi.org/10.1063/1.359446>.
23. Chen, M. & Porod, W. Design of gate-confined quantum-dot structures in the few-electron regime. *J. Appl. Phys.* **78**, 1050–1057, DOI: [10.1063/1.360339](https://doi.org/10.1063/1.360339) (1995). <https://doi.org/10.1063/1.360339>.
24. Darling, R. B. Defect-state occupation, fermi-level pinning, and illumination effects on free semiconductor surfaces. *Phys. Rev. B* **43**, 4071–4083, DOI: [10.1103/PhysRevB.43.4071](https://doi.org/10.1103/PhysRevB.43.4071) (1991).

25. Larkin, I. & Shikin, V. Diagnostics of individual quasi-one-dimensional electronic channels. *Phys. Lett. A* **151**, 335 – 338, DOI: [https://doi.org/10.1016/0375-9601\(90\)90293-W](https://doi.org/10.1016/0375-9601(90)90293-W) (1990).
26. Pekola, J. P. *et al.* Single-electron current sources: Toward a refined definition of the ampere. *Rev. Mod. Phys.* **85**, 1421–1472, DOI: [10.1103/RevModPhys.85.1421](https://doi.org/10.1103/RevModPhys.85.1421) (2013).

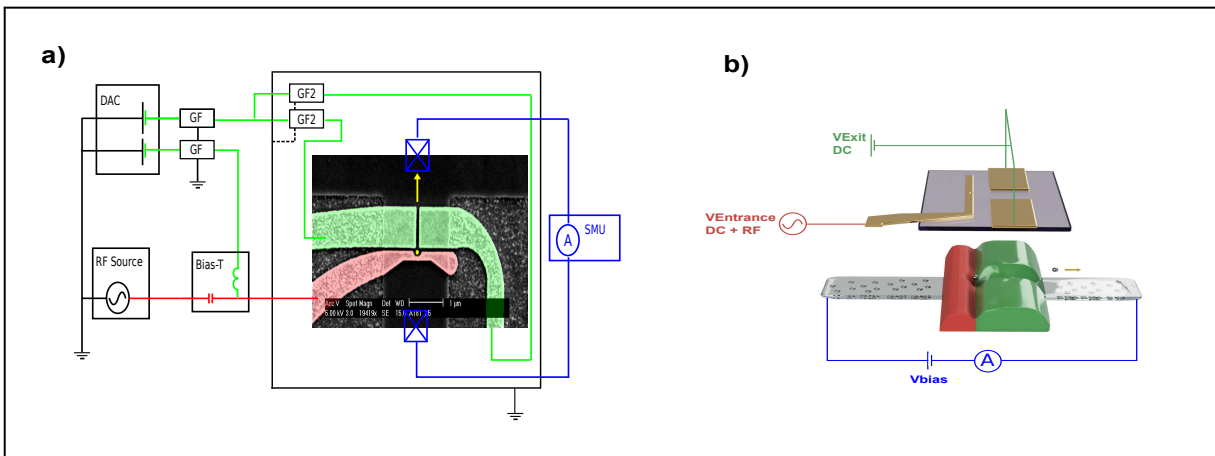


Figure 1. a) A false-colour scanning electron microscope (SEM) image of the pump device and a schematic of the measurement setup. b) Artists depiction of the dot potential formed by the finger gate potential (red) and saddle point potential (green) at the 2DEG formed by the split-gate pump.

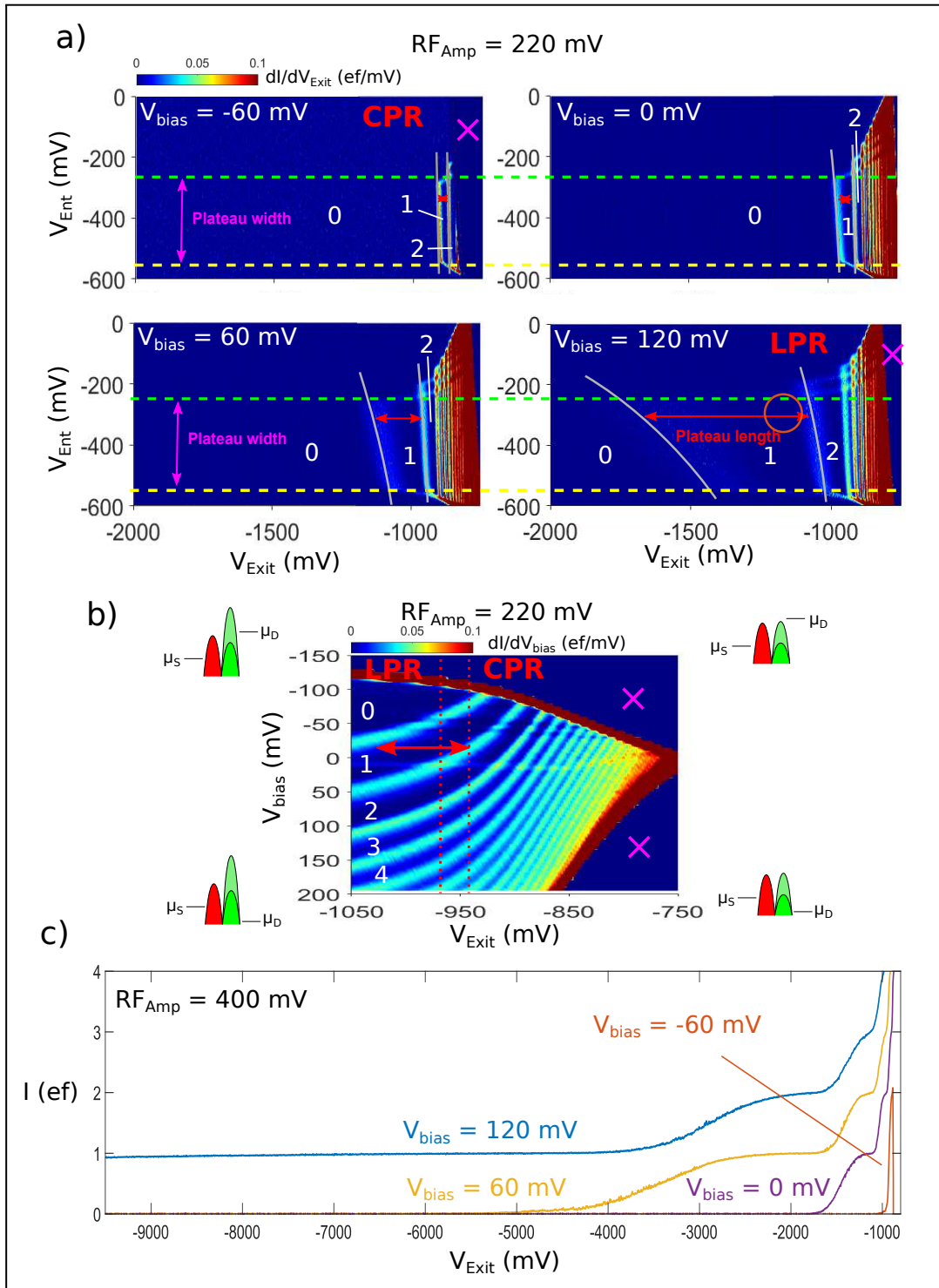


Figure 2. (a) Derivative pumpmaps at different source-drain voltage bias showing the transition between the CPR and LPR. The onset line (grey) is straight in the CPR and curved in the LPR. The number of pumped electrons per cycle are shown in white. (b) Derivative plot of current against V_{bias} and V_{Exit} . Schematics outside are a guide for the Derivative plot; they show the relative potentials of a cross section of a split-gate pump. (c) Linescans of pump plateaus at different source-drain voltage bias.

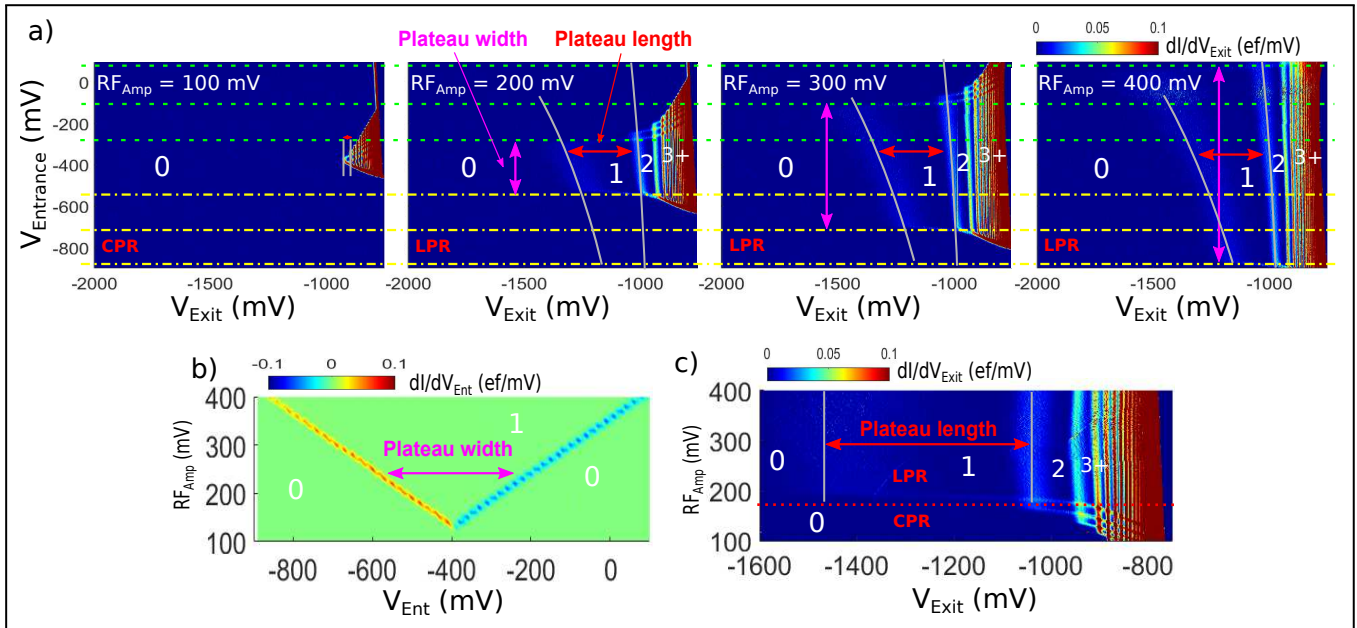


Figure 3. a) Derivative pumpmaps at different RF amplitudes. The number of pumped electrons per cycle are shown in white. Plateau length is the distance between the first and second onset lines (grey). Plateau width (purple arrow) is the distance between the capture lines (yellow dot-dashed) and ejection lines (green dashed). b) Derivative plot of current vs V_{Ent} and RF_{Amp} showing how plateau width changes with RF_{Amp} . The plateau width (purple) increases linearly with RF_{Amp} showing how plateau length changes with RF_{Amp} . c) Derivative pumpmap vs V_{Exit} and RF_{Amp}

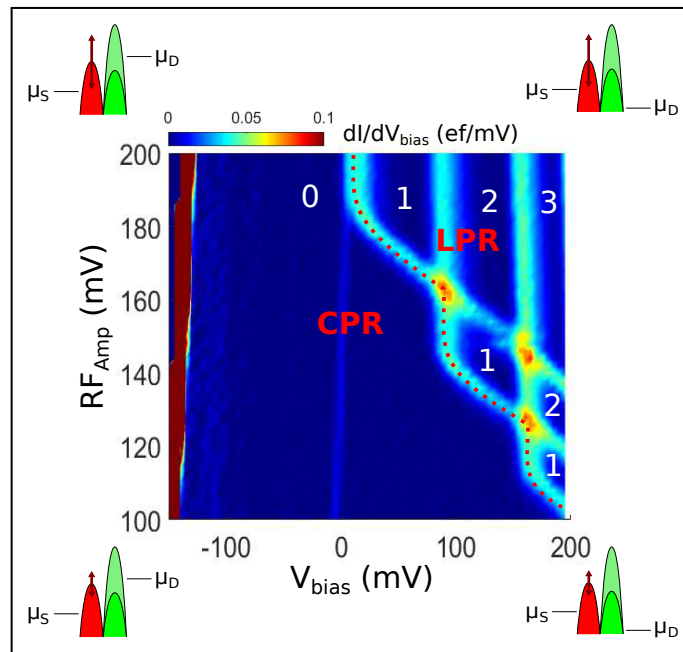


Figure 4. Derivative plot of current against V_{bias} and RF amplitude. The number of pumped electrons per cycle are shown in white. Schematics outside are a guide for the derivative plot; they show the relative potentials of a cross section of a split-gate pump.

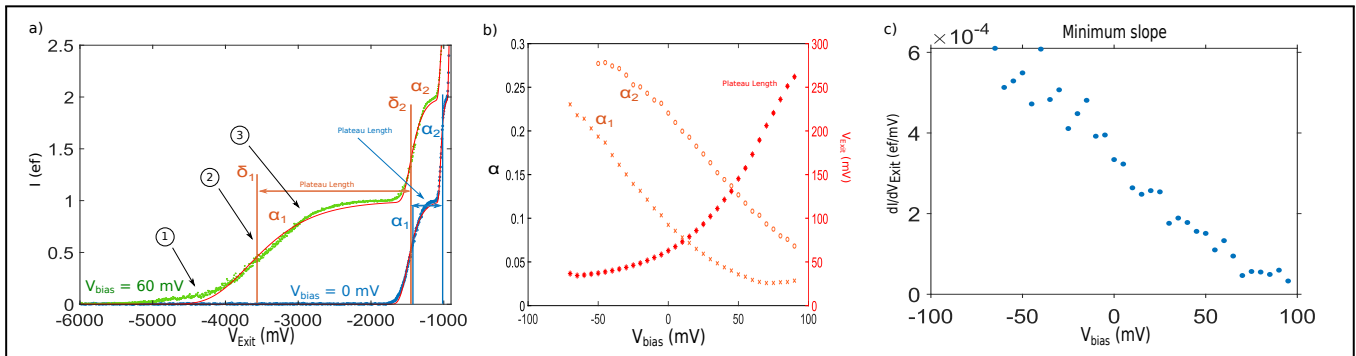


Figure 5. (a) UDC fits (red lines) to the linescans in the LPR. (b) Changes to α and plateau length from data in 2. (c) Minimum slope of the linescans from data in 2 for different V_{bias} .

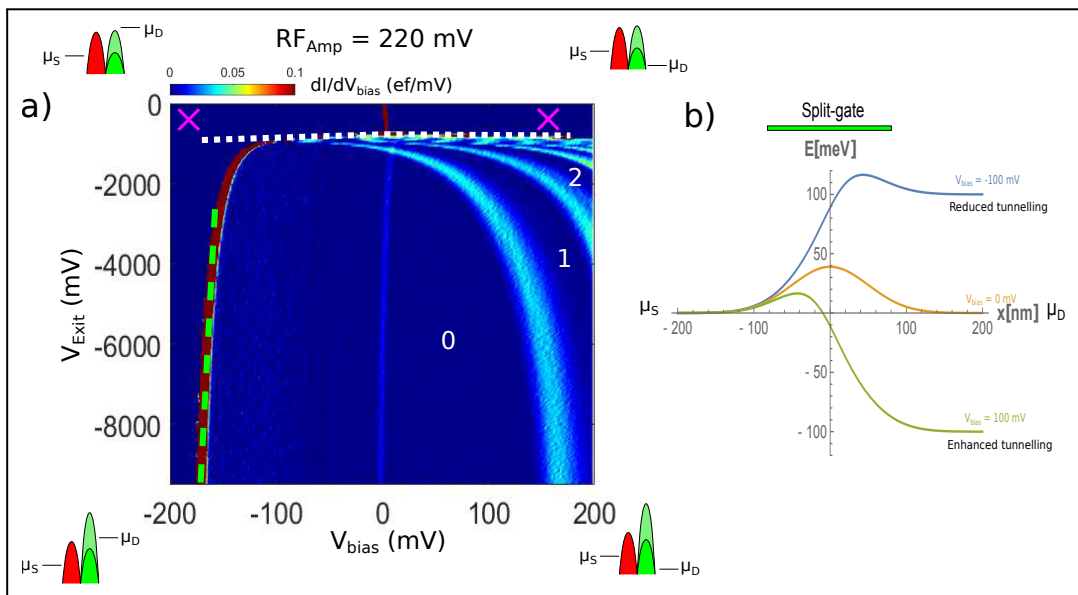


Figure 6. Derivative plot of current against V_{bias} and V_{Exit} . The regions marked by the purple 'X' show regions of Ohmic current. The dashed white line shows the transition from the Ohmic to pinched off pumping region in the CPR and the dashed green line shows the transition from the Ohmic to pinched off pumping region in the CPR, they are used to calculate the lever arm terms. (b) Electrostatic potential model of source drain bias effect on split-gate potential.

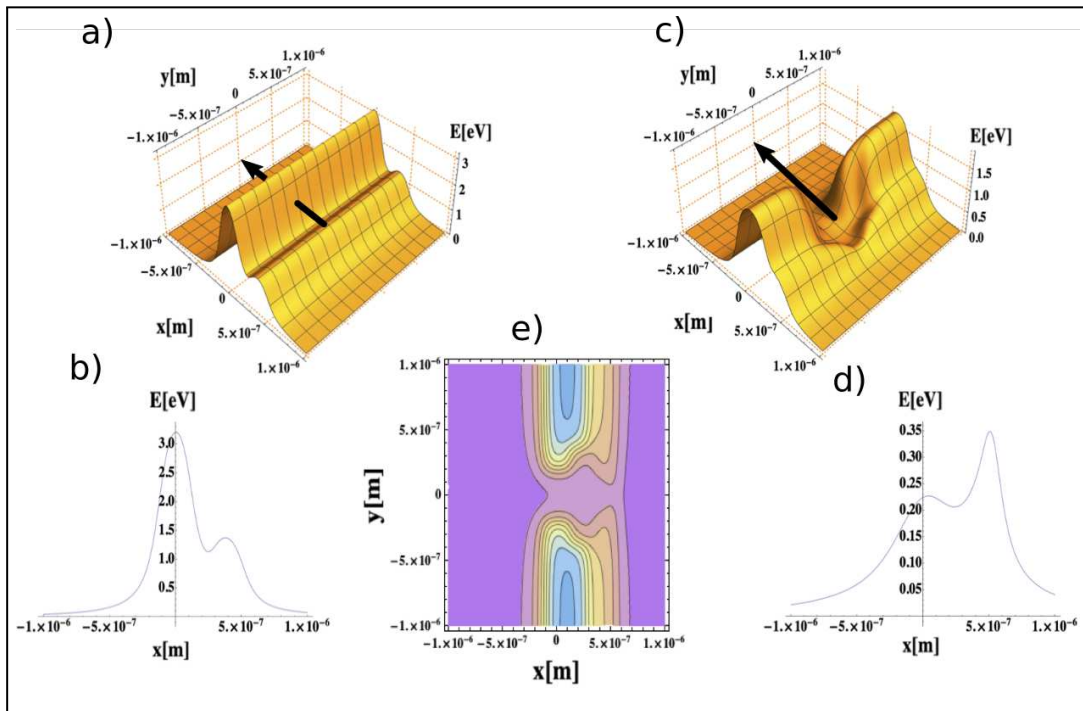


Figure 7. (a) Potential energy for finger-finger gate geometry. Black arrow indicates pump direction. (a) Cross section plot of finger-finger gate potential energy along the $y = 0$ line. With such a gate configuration there is no exit route for any captured electron. (c) Potential energy for finger-split gate geometry. Black arrow indicates pump direction. (d) Cross section plot finger-split gate potential energy along the $y = 0$ line. Here there is a clear exit route for any captured electron, through the saddle point of the exit gate. (e) Contour plot of the Potential energy for the finger-split gate geometry

Figures

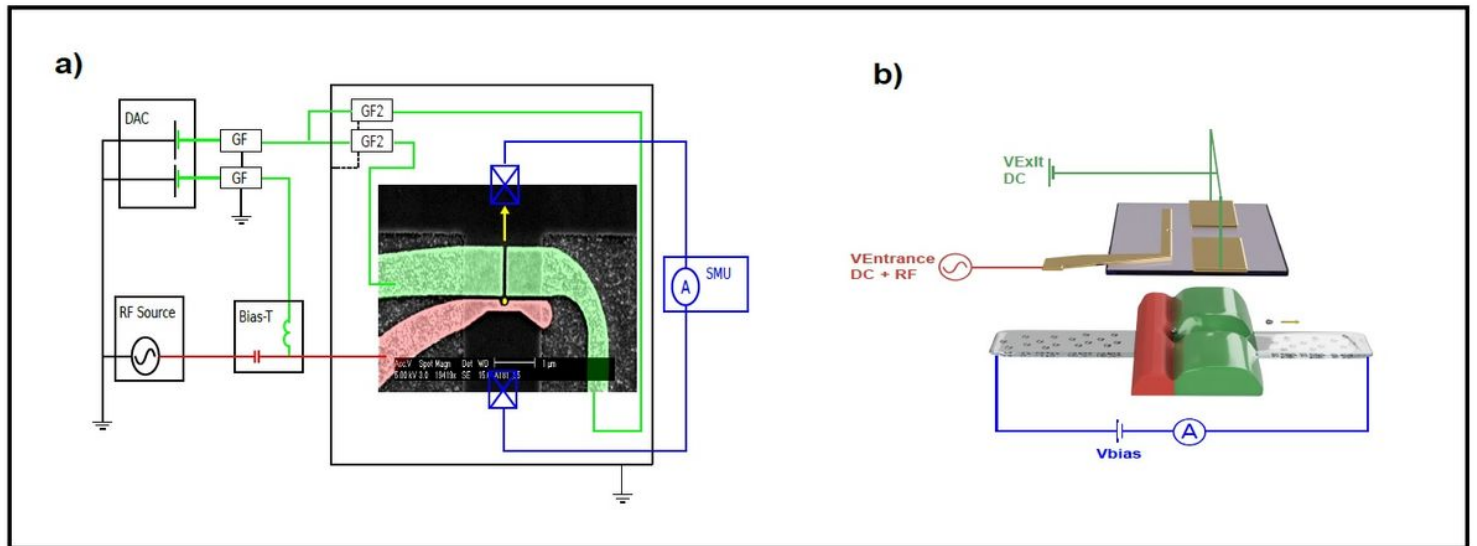


Figure 1

a) A false-colour scanning electron microscope (SEM) image of the pump device and a schematic of the measurement setup. b) Artists depiction of the dot potential formed by the finger gate potential (red) and saddle point potential (green) at the 2DEG formed by the split-gate pump.

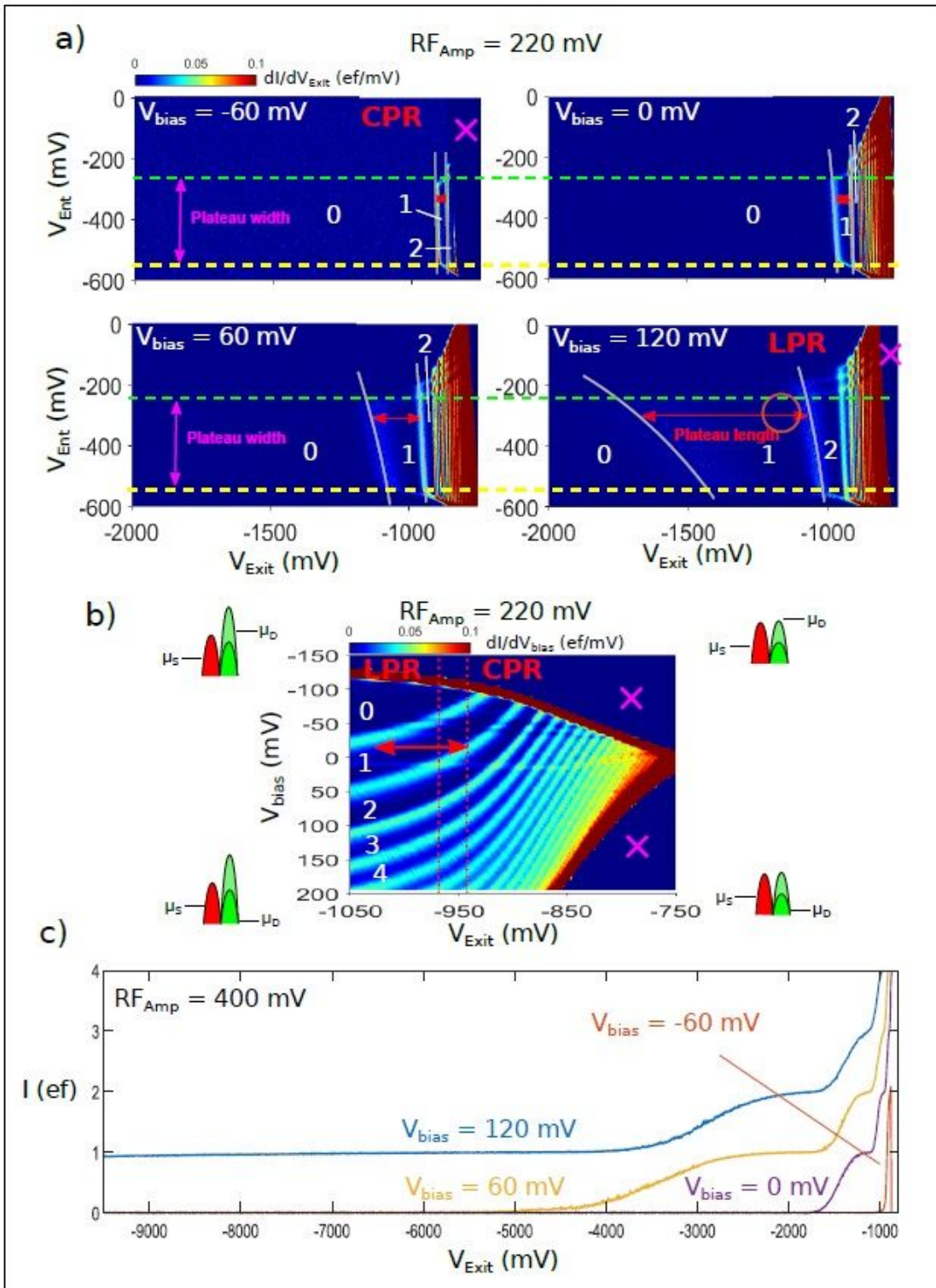


Figure 2

(a) Derivative pumpmaps at different source-drain voltage bias showing the transition between the CPR and LPR. The onset line (grey) is straight in the CPR and curved in the LPR. The number of pumped electrons per cycle are shown in white. b) Derivative plot of current against V_{bias} and V_{Exit} . Schematics outside are a guide for the Derivative plot; they show the relative potentials of a cross section of a split-gate pump. c) Line scans of pump plateaus at different source-drain voltage bias.

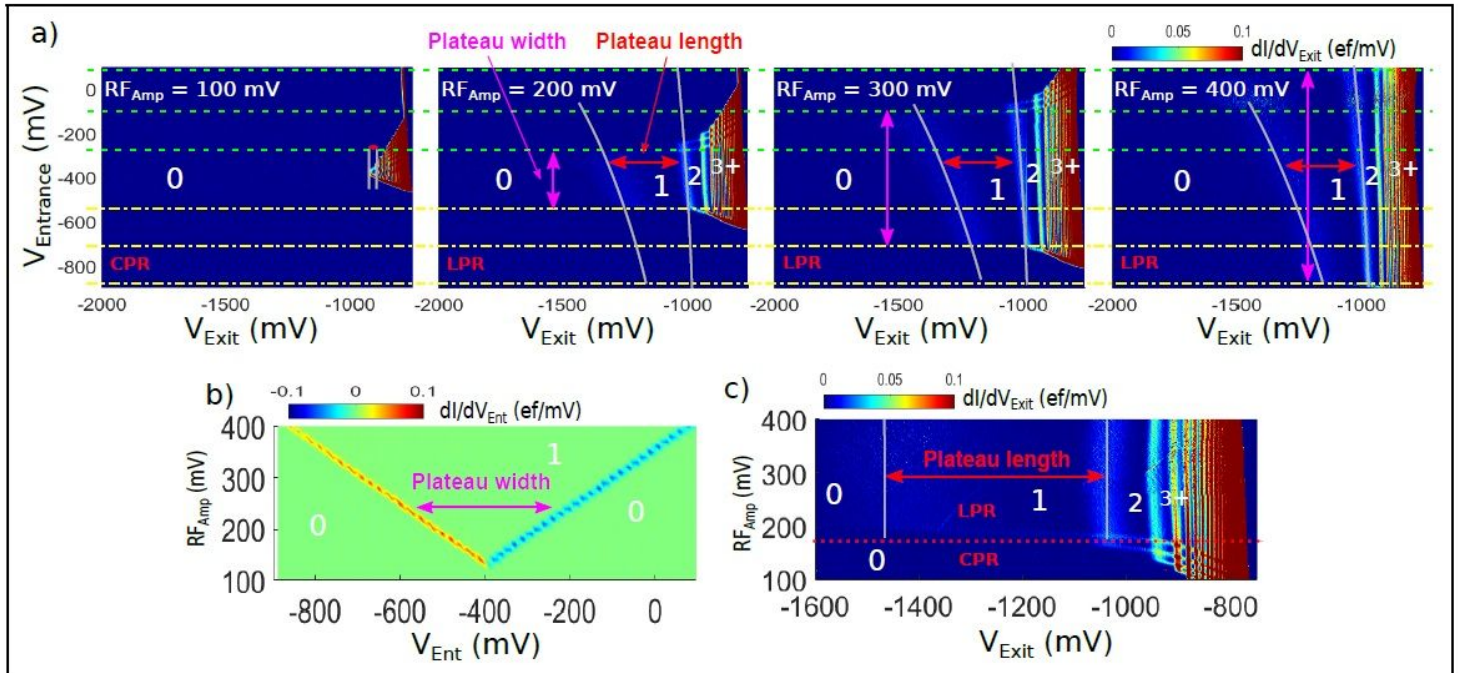


Figure 3

a) Derivative pumpmaps at different RF amplitudes. The number of pumped electrons per cycle are shown in white. Plateau length is the distance between the first and second onset lines (grey). Plateau width (purple arrow) is the distance between the capture lines (yellow dot-dashed) and ejection lines (green dashed). b) Derivative plot of current vs V_{Ent} and RF_{Amp} showing how plateau width changes with RF_{Amp} . The plateau width (purple) increases linearly with RF_{Amp} showing how plateau length changes with RF_{Amp} . c) Derivative pumpmap vs V_{Exit} and RF_{Amp}

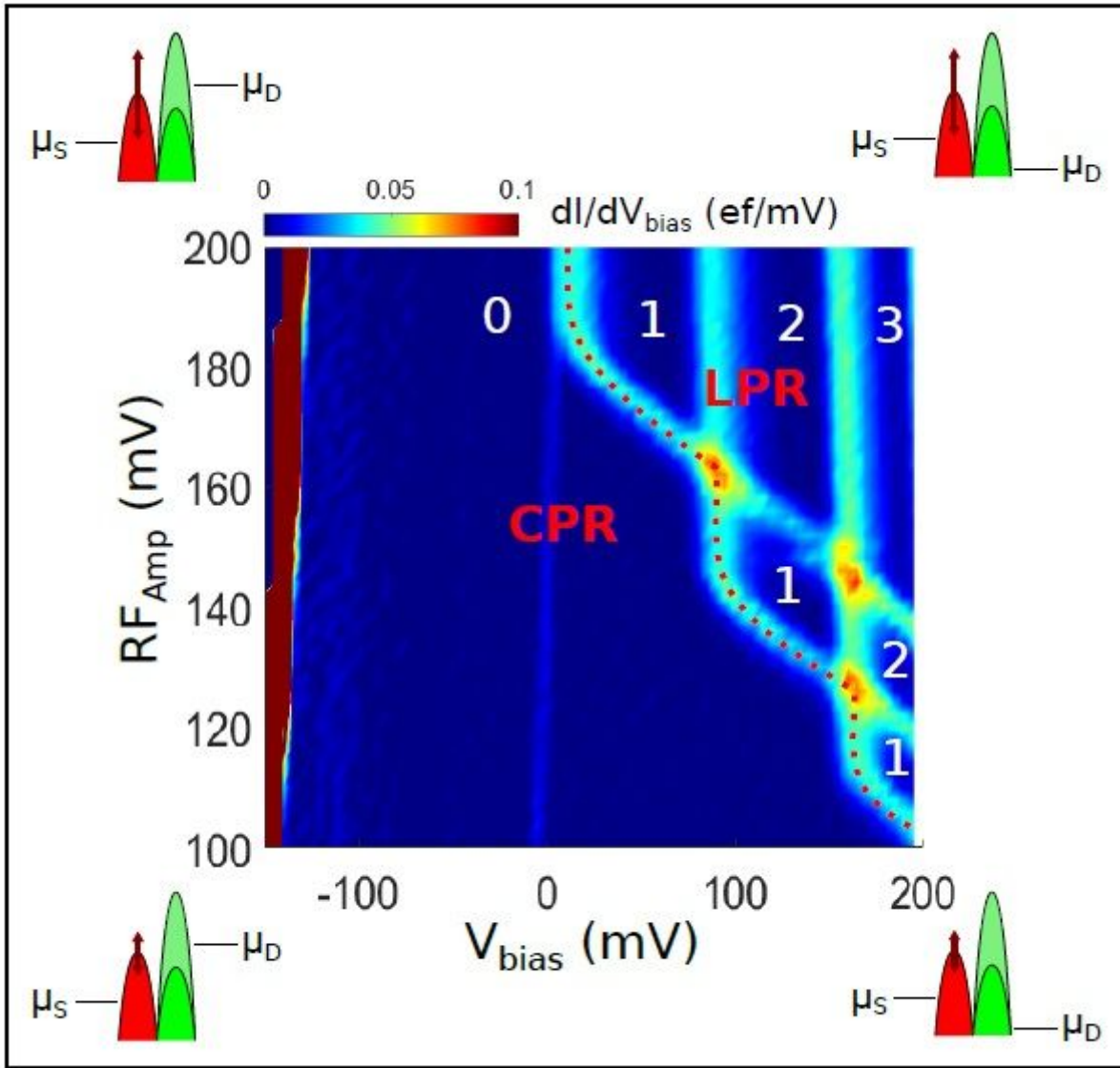


Figure 4

Derivative plot of current against V_{bias} and RF amplitude. The number of pumped electrons per cycle are shown in white. Schematics outside are a guide for the derivative plot; they show the relative potentials of a cross section of a split-gate pump.

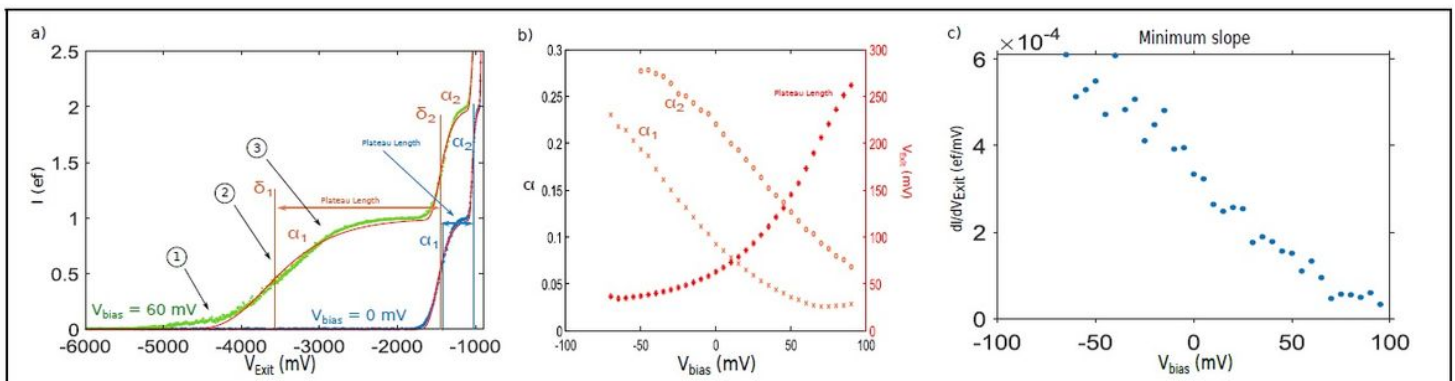


Figure 5

(a) UDC fits (red lines) to the linescans in the LPR. (b) Changes to a and plateau length from data in 2. (c) Minimum slope of the linescans from data in 2 for different V_{bias} .

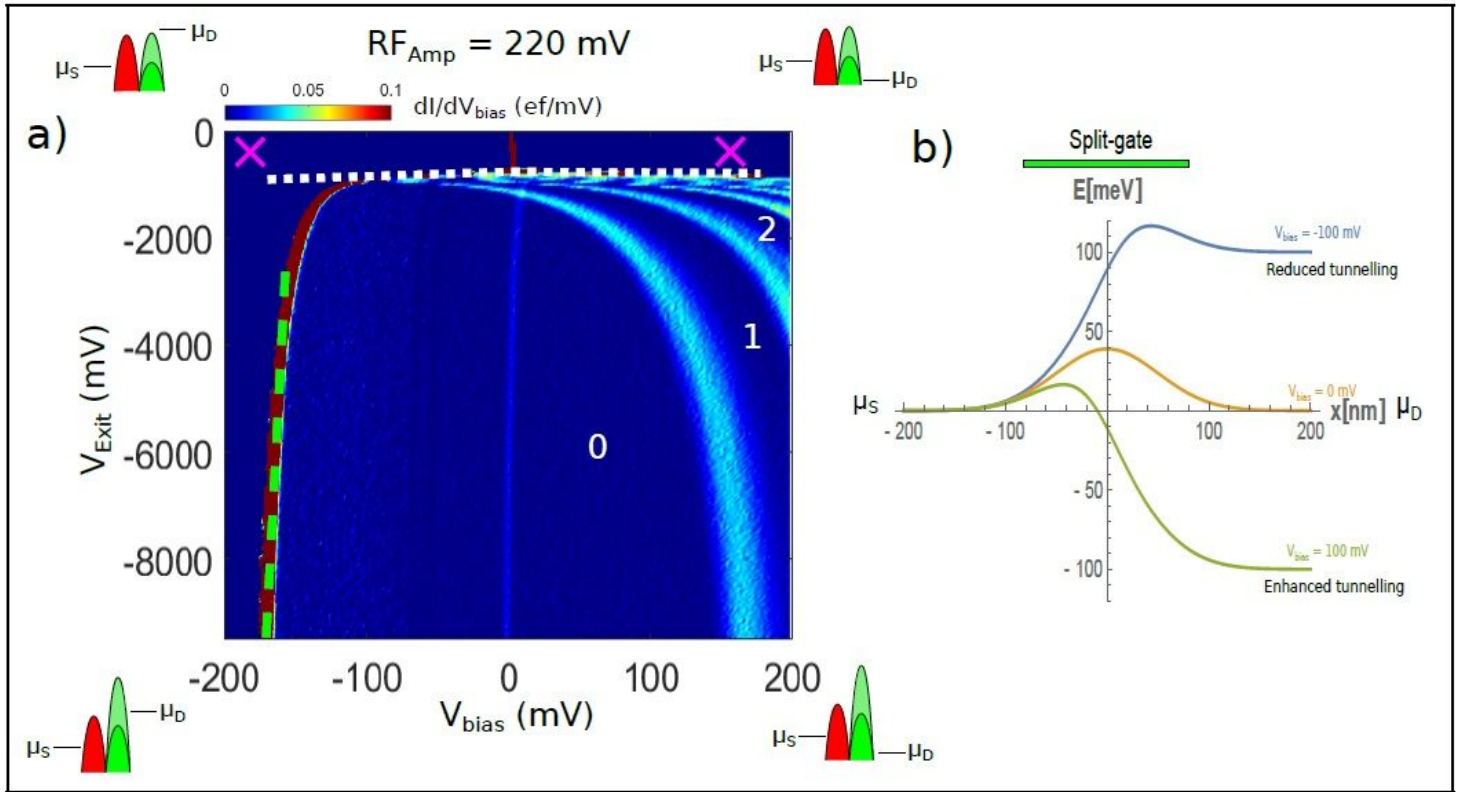


Figure 6

Derivative plot of current against V_{bias} and V_{Exit} . The regions marked by the purple 'X' show regions of Ohmic current. The dashed white line shows the transition from the Ohmic to pinched off pumping region in the CPR and the dashed green line shows the transition from the Ohmic to pinched off pumping region in the CPR, they are used to calculate the lever arm terms. (b) Electrostatic potential model of source drain bias effect on split-gate potential

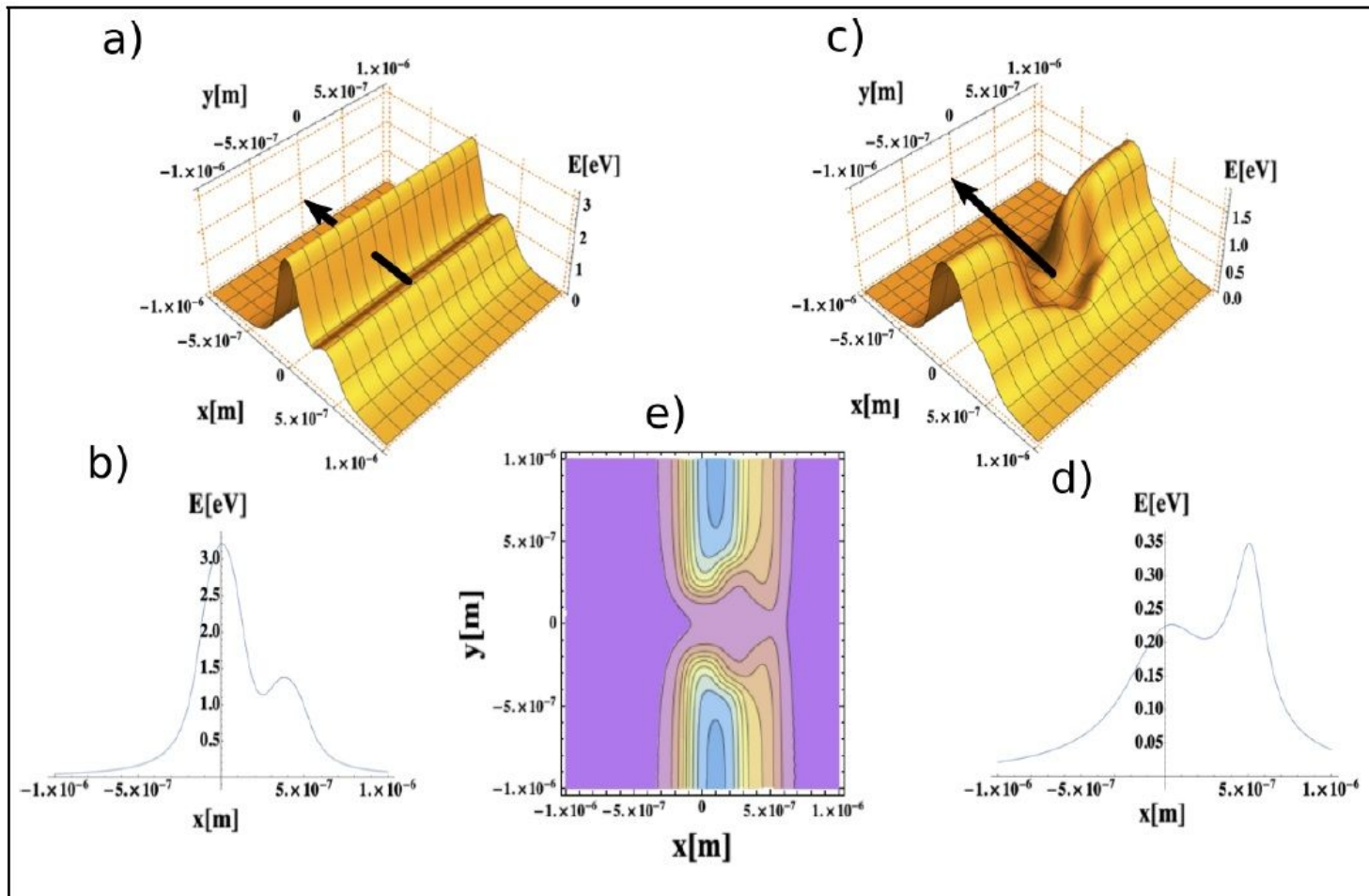


Figure 7

(a) Potential energy for finger-finger gate geometry. Black arrow indicates pump direction. (a) Cross section plot of finger-finger gate potential energy along the $y = 0$ line. With such a gate configuration there is no exit route for any captured electron. (c) Potential energy for finger-split gate geometry. Black arrow indicates pump direction. (d) Cross section plot finger-split gate potential energy along the $y = 0$ line. Here there is a clear exit route for any captured electron, through the saddle point of the exit gate. (e) Contour plot of the Potential energy for the finger-split gate geometry